ORIGINAL PAPERS

Increased solar-driven chemical transformations through surface-induced benzoperylene aggregation in dye-sensitized photoanodes

Didjay F. Bruggeman[1] · Remko J. Detz[2] · Simon Mathew[1] · Joost N. H. Reek[1]

Abstract

The impact of benzo[ghi]perylenetriimide (**BPTI**) dye aggregation on the performance of photoelectrochemical devices was explored, through imide-substitution with either alkyl (**BPTI-A**, 2-ethylpropyl) or bulky aryl (**BPTI-B**, 2,6-diisopropylphenyl) moieties, to, respectively, enable or suppress aggregation. While both dyes demonstrated similar monomeric optoelectronic properties in solution, adsorption onto mesoporous SnO_2 revealed different behavior, with **BPTI-A** forming aggregates via π-stacking and **BPTI-B** demonstrating reduced aggregation in the solid state. **BPTI** photoanodes were tested in dye-sensitized solar cells (DSSCs) before application to dye-sensitized photoelectrochemical cells (DSPECs) for Br_2 production (a strong oxidant) coupled to H_2 generation (a solar fuel). **BPTI-A** demonstrated a twofold higher dye loading of the SnO_2 surface than **BPTI-B**, resulting in a fivefold enhancement to both photocurrent and Br_2 production. The enhanced output of the photoelectrochemical systems (with respect to dye loading) was attributed to both *J*- and *H*- aggregation phenomena in **BPTI-A** photoanodes that lead to improved light harvesting. Our investigation provides a strategy to exploit self-assembly via aggregation to improve molecular light-harvesting and charge separation properties that can be directly applied to dye-sensitized photoelectrochemical devices.

Graphical Abstract

Increased Solar-Driven Chemical Transformations through Surface-Induced Benzoperylene Aggregation in Dye-Sensitized Photoanodes. Benzo[ghi]perylenetriimide (**BPTI**) dyes are investigated to reveal the effect of aggregation by π-stacking on photovoltaic parameters in dye-sensitized devices. Photoanodes with aggregating **BPTIs** show both J- and H- aggregation


✉ Joost N. H. Reek
j.n.h.reek@uva.nl

1 Homogeneous, Supramolecular and Bioinspired Catalysis, van 't Hoff Institute for Molecular Sciences, University of Amsterdam, Science Park 904, 1098 XH Amsterdam, The Netherlands

2 Energy Transition Studies, Netherlands Organization for Applied Scientific Research (TNO), Radarweg 60, Amsterdam, The Netherlands

phenomena leading to enlarged visible light absorbance and increased electron injection. The use of aggregating **BPTI** outperforms a non-aggregation **BPTI** with fivefold in terms of photocurrent and product generation.
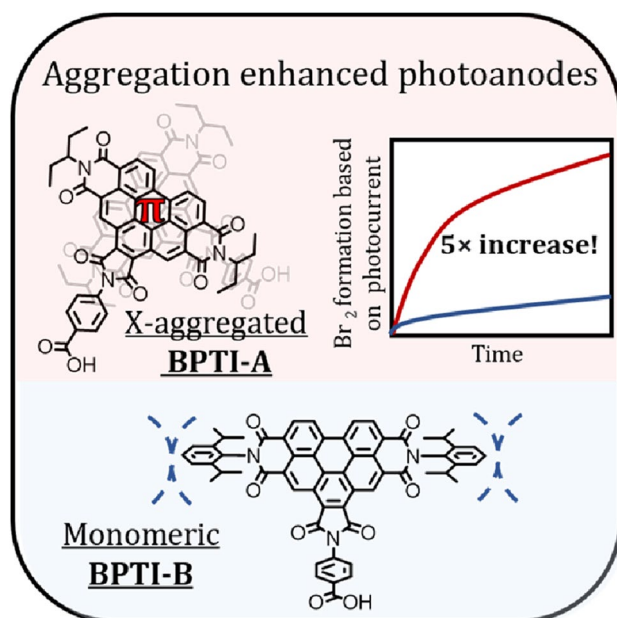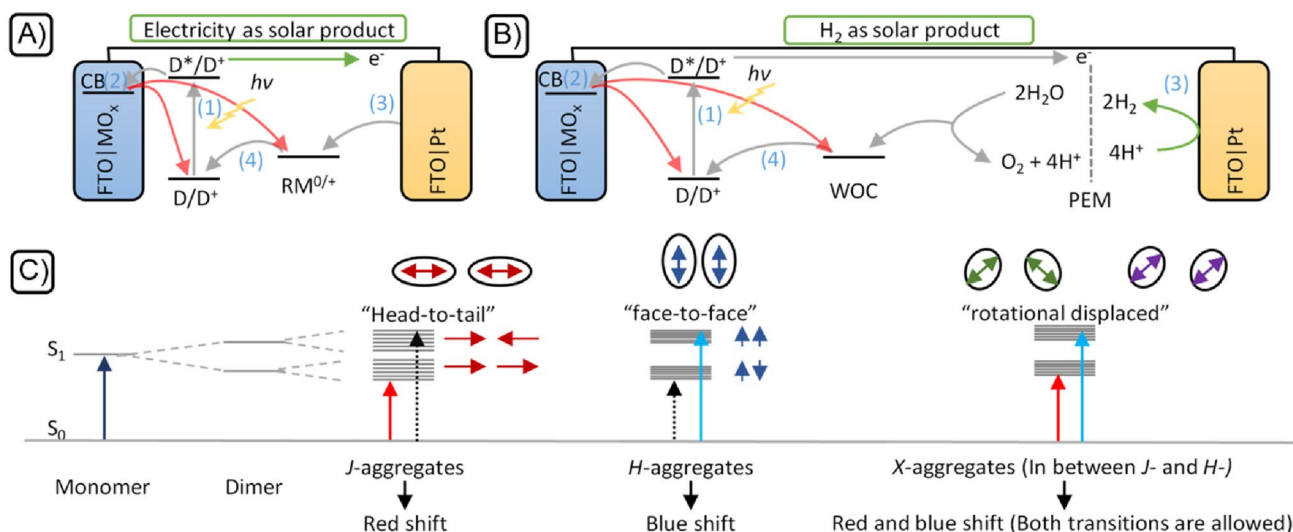
1 Introduction

The emissive nature of fossil fuels continues to stimulate interest in next-generation renewable energy technology [1]. Renewable "solar fuel" can be generated indirectly by collecting solar energy (i.e., photovoltaics) and storing electrical energy within chemical bonds via electrochemical reactions (i.e., electrolysis) [2]. In contrast, photosynthesis uses a direct approach to convert solar energy into chemical energy (i.e., sugars), with molecular components for light-harvesting, electron transport, redox mediation, and catalysis [3]. From this, we are inspired to realize "artificial photosynthesis" combining light-harvesting with redox transformations to generate fuel products [4]. Dye-sensitized photoelectrochemical cells (DSPECs) expand the capabilities of dye-sensitized solar cells (DSSCs) to catalytic conversion processes i.e., to direct light-driven production of fuels. As depicted in Scheme 1A, DSSCs generate photocurrent (i.e., electricity) by employing molecular dyes (1) to harvest light, wide-bandgap semiconductors (2) to transport electrons, and redox mediators (RMs, 3 and 4) to shuttle electrons between the cathode and photooxidized dye (D^+), closing the circuit [5–7]. In contrast, Scheme 1B outlines a (typical) DSPEC, featuring

separate photoanode and cathode compartments to enable catalytic oxidative (4) and reductive (3) transformations [8, 9]. Specifically, Scheme 1B depicts a DSPEC solar-to-fuel device, where the initial steps of light absorption and charge injection are the same as a DSSC, but featuring a water oxidation catalyst (WOC) at the photoanode to regenerate D^+ and provide protons for fuel-forming catalytic transformations (i.e., H^+ or CO^2 reduction) at the cathode [10, 11]. Water-splitting DSPECs exhibit low efficiencies [12] as four high-potential (E_{woc} = > 1.23 V *vs.* NHE) [13] redox equivalents are required for one catalytic cycle, creating a kinetic competition between catalysis and charge recombination pathways (red arrows) [14].

Different strategies have been investigated to suppress recombination, including insulating layers over the metal oxide (MO_x) [16], increasing the catalyst–MO_x linker length [17], and introducing redox-relays between dye–catalyst components [18, 19]. Recently, electron/hole shuttles in the form of redox-active molecules have been introduced to suppress recombination [20], and we envision utilizing this approach in a DSPEC to generate a long-lived, mobile chemical-oxidant that can drive a solution-based WOC. With this approach, proximity between the WOC and the surface-mounted dye is not required, eliminating the aforementioned recombination pathways hampering WOC operation [21],
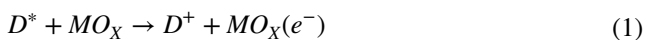
Scheme 1 A Schematic representation of an operating DSSC for electricity production and **B** DSPEC for H$_2$O oxidation and H$_2$ production. **C** Simplified scheme of exciton theory for different absorption behaviors of *H-, J-,* and *X*-aggregates [15]. D = dye, D$^+$ = oxidized dye, D* = excited dye), *CB* conduction band, *MO$_x$* metal oxide, *WOC* water oxidation catalyst, *RM* redox mediator, and *e$^-$* electrons

as electron transfers from the WOC to D$^+$ are diffusional, akin to RM shuttling between photoanode and cathode in DSSCs. Furthermore, the use of a redox shuttle also optimizes D$^+$ regeneration, as the sluggish kinetics of WOC do not limit D$^+$ regeneration [22]. An attractive candidate for a redox shuttle is the Br$^-$/Br$_2$ couple, featuring a high oxidation potential (*E*ox) of 1.1 V *vs*. NHE in water (pH 1–5.4) [20, 22, 23]. Previous studies established that molecular ruthenium WOCs can oxidize water with in situ-generated Br$_2$ (generated from a Br$^-$/Br$_2$ redox couple) as a sacrificial oxidant [20].

In a complementary fashion, the Br$^-$/Br$_3^-$ couple is already established as a high RM in *n*-type DSSCs [22–24]. Br$_2$ could be generated by oxidation of the Br$^-$ in aqueous HBr solutions by the photooxidized dyes (Eq. 1–4) [22, 25]. Even though the oxidation of Br$^-$ is kinetically favorable, strongly oxidizing dyes are still necessary. Additionally, recent studies show that Br$_2$ generated in PECs can be used for the oxidation of alkenes [26]. This opens the field for new strategies to produce value-added chemicals coupled with solar fuel generation.

$$D^* + MO_X \rightarrow D^+ + MO_X(e^-) \tag{1}$$

$$D^+ + 2Br^- \rightarrow D + Br_2^- \tag{2}$$

$$2Br_2^- \rightarrow Br_3^- + Br^- \tag{3}$$

$$Br_3^- \leftrightarrow Br_2 + Br^- \tag{4}$$

Br$_2$ formation in DSPECs requires an aqueous environment with low pH [27], which can be detrimental to photoanodes stability when (commonly used) carboxylic acid anchoring groups are employed [28]. While this can be ameliorated by special surface treatments (i.e., ALD) [29, 30], the issue can be bypassed by using dyes that do not require a molecular linker [27, 31]. In this context, systems featuring MO$_x$ sensitization via exploiting π-stacking and hydrophobic forces of photosensitizers—notably perylene dyes—is interesting [27, 31]. Using aggregation as a construction tool appears counterintuitive, as dye aggregation is typically viewed as an undesirable phenomenon in DSSCs for several reasons. Additional dye layers on top of chemisorbed monolayers are thought to detract from (photocurrent producing) light harvesting by not participating in electron injection. These "photovoltaically inactive" dye-aggregates can prevent the RM from regenerating D$^+$, and the illumination of dye molecules in close proximity to each other can result in intramolecular excited-state quenching that diminishes electron injection [32]. In contrast to these observations in synthetic systems, Nature's photosystems employ the precise placement of several dyes to improve light-harvesting properties, with the self-assembled chlorophyll stacks in the light-harvesting systems demonstrating exciton stabilization over distances up to 10–15 nm, inspiring recent efforts to exploit dye aggregation for improved DSSC light harvesting [33].
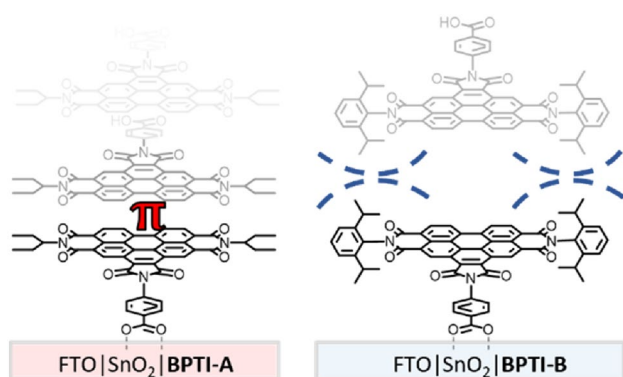
Scheme 2 Proposed chemisorption and aggregation modes of **BPTI-A** and **BPTI-B** on FTO|SnO$_2$. Aggregation of **BPTI-A** is visualized as *H*-aggregation for clarity. Discussion on aggregation mode is elaborated in Scheme 1C and Sections S8–9 in the SI [15]

Specific modes of aggregates can exhibit a hypsochromic shift (*H*-aggregation, Scheme 1C) that reduces light harvesting[15] or a bathochromic shift (*J*-aggregation, Scheme 1C) that improves light harvesting in devices [34]. However, aggregates that show properties of both *H*- and *J*- aggregates (*X*-aggregates [35], Scheme 1C) are also possible [15, 35–37]. Herein, we explore the role of dye aggregation in mesoporous SnO$_2$ semiconductor photoanodes. We investigated the effect of aggregation on the photovoltaic performance and stability in aqueous DSSCs before demonstrating efficient Br$_2$ formation in DSPECs. We present here two novel benzo[ghi]perylenetriimide (**BPTI**, Scheme 2) dyes derived from perylenediimides (**PDIs**) [38, 39] with more expanded π-conjugated systems in the bay area leading to π-systems that can access high oxidation potentials (> 2.0 V *vs*. NHE)[38, 39]. These dyes are hydrophobic, and strong π–π interactions yield stable photoanodes for highly oxidative, aqueous phase redox reactions. Photoanodes containing the *X*-aggregating **BPTI-A** demonstrated a fivefold increase in photocurrent production in DSSCs compared to the non-aggregating **BPTI-B.** This result is translated to the DSPEC-based formation of Br$_2$ coupled to cathodic H$_2$ production. The **BPTI**-dyes are light, water, and air-stable, both in solution and on semiconductor surfaces [38, 39].

2 Results and discussion

2.1 Synthesis and characterization of BPTIs

(**B**)**PTIs** are known to self-assemble to (multimeric) aggregated species through π–π stacking of monomers and in various orientations, as shown in Scheme 1C

[40–42]. To promote aggregation, the **BPTI**s were functionalized with either an **A**lkyl (**BPTI-A**) chain (2-ethylpropyl) at both imide positions to maintain the flat π-system or a **B**ulky (**BPTI-B**) aryl group (specifically 2,6-diisopropylphenyl) prevent π-stacking by which are often utilized to suppress π-stacking by increasing steric hindrance to favor a monomeric species [43].

Both **BPTI** dyes were synthesized from the respective parent **PDI-A/B** (i.e., featuring the respective imide substituents, SI **Scheme S1**) via Diels–Alder cyclization at the perylene bay region with maleic anhydride in the presence of *p*-chloranil to yield **BPTI**s with anhydride functional groups while extending the aromatic system, as we anticipate that a greater π–π interaction will promote aggregation [44]. Finally, the installation of a benzoic acid anchoring group for chemisorption onto MO$_x$ was achieved via condensation with 4-aminobenzoic acid, to yield **BPTI-A** and **BPTI-B**. The main role of the carboxylic acid unit is to ensure similar initial dye–MO$_x$ attachment (angle, 1 or 2 oxygen biding, and distance of the protonated surface, etc.) to limited infare key aspects that rule a better electron injection and is elaborated on in SI section S11. Both **BPTI**s are yellow–orange in color and sparingly soluble in organic solvents (THF, CHCl$_3$), enabling characterization by ¹H-NMR (@40 °C), HR−MS, and FT−IR spectroscopy (SI, Section S3).

2.2 Electrochemical investigation of BPTIs in solution

The solution electrochemistry of monomeric **BPTI**s was examined to assess the influence of alkyl/aryl imide substitution on redox potentials. Cyclic voltammetry (CV, Fig. 1A) of **BPTI**s in DMF was used to determine the potential of the 1st reduced species, summarized in Table 1. The 1st reduced species can be used to estimate the LUMO [45, 46], although 2nd and 3rd reduced species are observed and known for similar compounds, [38, 39] with the quantity of the reduced species of (**B**)**PTI**s known to depend on the number of imides [47]. A slight negative shift of ~ 100 mV is observed between the reduction potentials (*E*red) of the **BPTI-A** and **BPTI-B** (*E*$_{red}$ = − 0.27 and − 0.19 *vs*. NHE, respectively), likely due to the electron-donating alkyl and the electron-withdrawing aryl imide substituents. Although this potential difference is small, it may affect the device's properties as the greater reducing power of **BPTI-A** excited state (**BPTI-A***) may result in faster electron injection into the SnO$_2$ conduction band (CB) [39, 48, 49]. The limited electrochemical window of DMF precluded the determination of *E*$_{ox}$, required to estimate the level of the highest occupied molecular orbital (HOMO) of the dye [45], which typically is used to estimate the oxidative power generated at **BPTI**-sensitized photoanodes by photo-oxidation of the dye
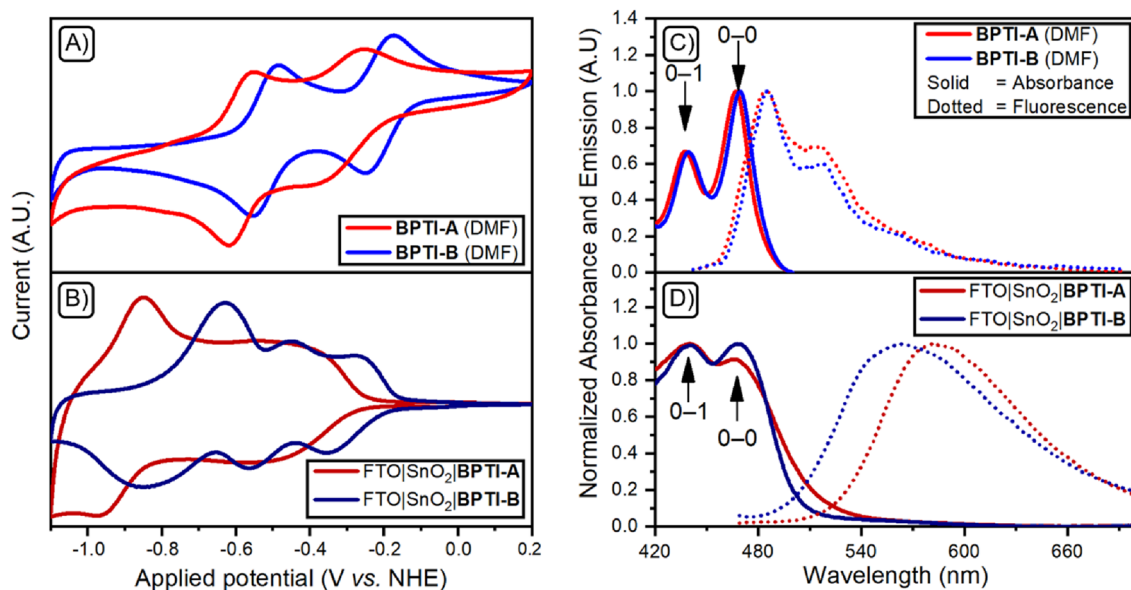
Fig. 1 **A** CV scans of **BPTI-A** (red) and **BPTI-B** (blue) in 100 mM TBAPF$_6$ DMF (~0.25 mM) and **B** FTO|SnO$_2$|**BPTI-A** (dark red) and **BPTI-B** (dark blue) in (100 mM TBAPF$_6$ in MeCN). Normalized absorbance spectra and fluorescence spectra (solid lines = absorption, dotted lines = emission) of **C** **BPTI-A** (red) and **BPTI-B** (blue) in DMF (μM) and **D** FTO|SnO$_2$|**BPTI-A** (dark red) and **BPTI-B** (dark blue) with λ$_{ex}$ = 420 nm (measurements are shown from 420 nm to prevent SnO$_2$ absorption)

Table 1 Summary of optical (C = μM, λ$_{ex}$ = 420 nm,) and electrochemical properties (100 mM TBAP, 0.25 mM) of **BPTI-A** and **BPTI-B** in DMF (D = dye, ~0.25 mM) and FTO|SnO$_2$|**BPTI-A** and **BPTI-B**

Entry	Compound	λ$_{abs}$	$\frac{0-0}{0-1}$ abs	E	λ$_{em}$	$\frac{0-0}{0-1}$ em	Δλ	E_{0-0}	E_{red}	E_{ox}
1	**BPTI-A**	467	1.39	49,208	485	1.44	18	2.61	− 0.27	2.17[a]/2.34[b]
2	FTO|SnO$_2$|**BPTI-A**	465	0.93	–	580	–	115	2.38	− 0.23	2.15[b]
3	**BPTI-B**	469	1.49	51,228	485	1.71	16	2.60	− 0.19	2.27[a]/2.41[b]
4	FTO|SnO$_2$|**BPTI-B**	468	1.03	–	560	–	92	2.47	− 0.17	2.30[b]

Maximal absorbance wavelength of the 0–0 transition (λ$_{abs}$), maximal emission wavelength of the 0–0 transition (λ$_{em}$) and Stokes shift (Δλ) in nm. Ratio peak height of the 0–1 and 0–0 transition in absorbance ($\frac{0-0}{0-1}$ abs) and emission ($\frac{0-0}{0-1}$ em) dimensionless. Molar extinction coefficient of the 0–0 transition (ε) in M^{-1} cm^{-1} Estimation of the optical gap by the zero–zero spectroscopic energy (E_{0-0}) in eV. 1st reduction (E_{red}, D/D$^-$) and oxidation potential (E_{ox}, D/D$^+$) of the dyes (D) in V vs. *NHE*

[a] D/D$^+$ measured in 100 mM benzonitrile or [b] D/D$^+$ calculated with HOMO = LUMO + $E0-0$ with the first reduction potentials (E_{red}) [45], corresponding to the LUMO level [51].

[50, 51]. Therefore, differential pulse voltammetry (DPV, **Figure S9**) was performed in benzonitrile, which revealed an E_{ox} at 2.17 V and 2.27 V and a lower Ered at − 0.37 V and − 0.27 V vs. NHE for **BPTI-A** and **BPTI-B**, respectively. These values are slightly lower than the calculated HOMO using the zero-zero spectroscopic energy (vide infra), which is likely due to the general potential shift caused by changing the solvent. While two distinct, reversible redox events—corresponding to the mono- and direduced species—are apparent for both dyes [43], the 1st reduction of **BPTI-A** (E_{red} = − 0.27 vs. NHE) exhibits a notable broadening compared to the sharp analogous redox wave of **BPTI-B** (E_{red} = − 0.19 vs. NHE). Therefore, scan-rate dependent measurements (**Figure S10**) of both **BPTIs** were performed,

excluding electrochemical irreversibility as the origin of the broadness of the 1st **BPTI-A** reduction waves. Broadness in redox waves is often seen in redox polymers [52], and is likely a superposition of multiple sharp redox waves attributed to slightly different redox levels that arise from dye–dye interactions as a result of aggregation [48], suggesting that **BPTI-A** self-assembles at concentrations employed in electrochemical studies. It is important to note that the CVs are recorded at mM **BPTI** concentration ranges, three orders of magnitude greater than those used in spectrophotometric studies (vide infra). We came to notice that **BPTI-A** affords a saturated solution at 0.25 mM, while **BPTI-B** can be dissolved in concentrations up to 10 mM.

The electrochemistry of **BPTI** in solution was investigated to assess the effect of alkyl/aryl imide substitution on redox potentials reflecting the HOMO and LUMO, and only a minor negative shift in reduction potentials between **BPTI-A** and **BPTI-B** was found.

2.3 Solution-based spectrophotometry of the BPTI dyes

The ground-state electronic properties of the **BPTI** dyes were assessed by UV–Vis spectroscopy, measured in DMF solution, and upon immobilization on SnO_2 photoanodes (Fig. 1C–D) and summarized in Table 1. The monomeric (i.e., not aggregated) nature of both **BPTI** dyes at the concentrations used was confirmed titrations over the 0.1–10 mM range (**Figure S8**) to reveal a linear molar extinction coefficient (i.e., not showing *H*-, *J*- or *X*-bands, vide infra) [40, 41] Both **BPTIs** demonstrate three (**Figure S7**), well-resolved vibronic bands for the electronic transition of the ground singlet state (S_0) to the first excited singlet state (S_1), characteristic of planar π-conjugated **PDI** molecules [53, 54]. **BPTI-A** features absorption at 413, 438, and 467 nm, while **BPTI-B** exhibits slight bathochromic shifts, with maxima at 414, 439, and 469 nm. Calculation of the molar extinction coefficient revealed that the 0–1 and 0–0 bands of **BPTI-B** experience a slight (~ 10%) enhancement over **BPTI-A**. The similarities in absorbance spectra indicate that the aromatic substituent on the imide (imide is an electronic node[55]) of **BPTI-B** exerts a negligible influence on the π-system of the **BPTI** molecule [56]. The normalized steady-state fluorescence spectra (DMF concentration, ~ 1 μM) are presented in Fig. 1C–D and summarized in Table 1. Both **BPTIs** reveal emission that is a mirror-image of the absorbance spectra, reinforcing that imide substituents have a negligible influence on **BPTI** electronic structure. While the 0–0 emission band remains identical between the dyes, the 0–1 vibrational emission band of **BPTI-A** experiences a slight enhancement, leading to a (0–0/0–1) ratio between the two emission bands of 1.45 and 1.70 of **BPTI-A** and **BPTI-B**, respectively. The difference in the (0–0/0–1) ratio apparent in fluorescence spectra illustrates the different degrees of equilibria between **BPTI** monomer and aggregates (SI, Section S9, **Figure S23**) [44]. Experimental investigation on the solvatochromism of the **BPTIs** with various solvents with different dielectric constants (SI, Section S10, **Figure S24,** and **Table S3**) reveals an increase in Stokes shifts in solvents with a higher dielectric constant ($CHCl_3 = 6$ nm → DMF = 18 nm). In general, such a solvatochromism of the emission band is taken as an indication for stabilization of the excited state by increased polarity. The HOMO–LUMO gap was approximated using the zero–zero spectroscopic energy (E_{0-0}) to estimate the optical gap. The intersection of normalized absorption and emission data revealed that the estimated E_{0-0} of both dyes was found to be near-identical (~ 2.60 eV, Table 1), reinforcing that the frontier orbitals of **BPTI** dyes are not influenced by the imide substituent.

The ground-state electronic properties of **BPTI** dyes in solution were examined, indicating that they are monomeric by demonstrating a linear molar extinction coefficient, and we established that the imide substituent has no influence on the frontier orbitals of **BPTI** dyes.

2.4 Immobilization and characterization of BPTIs on SnO₂

Previously reported **BPTIs** were sensitized onto TiO_2-based photoanodes, creating an energetic mismatch between the lower unoccupied molecular orbital (LUMO) of the dye (− 0.2 eV) and the CB of the *n*-type semiconductor (− 0.5 eV) precluding electron injection in the device [38, 39]. Therefore, we utilized SnO_2 photoanodes as the low (− 0.05 eV) CB of this particular MOx sensitized should promote exergonic electron transfer from the excited **BPTI** dyes to the semiconductor.

BPTIs were chemisorbed onto FTO|SnO_2 photoanodes using a 0.25 mM solution (i.e., near-saturated for **BPTI-A**) using an adsorption time of 16 h. The influence of immobilization (and aggregation) on the electrochemical properties of FTO|SnO_2|**BPTI** photoanodes was probed by CV (Fig. 1B) in MeCN (the same solvent is used for DSSCs, vide infra), with the data summarized in Table 1. Employing the same aqueous working electrolyte used for Br_2 formation in DSSCs and DSPECs (0.1 M HBr, pH = 0.54, vide infra) was not possible, as the reduction of Sn^{4+} occurred prior to the **BPTIs** under these conditions [57]. Previous studies established that solvent/pH variations do not impact **BPTI** redox properties [31], prompting us to acquire data at pH 5.4 (**Figure S13**). Probing the **BPTI** oxidation on FTO|SnO_2 electrodes was impossible (even with PhCN solvent) as applied oxidation potentials induced dye desorption. We estimated these potentials using the optical gap (vide infra), in conjunction with the 1st reduction (although higher reductions are also possible, vide supra) [38, 39]. The CV of a reversible redox active substance that is confined/immobilized on the working electrode surface differs from that of freely diffusing species. Materials with slower electron transfer show complex behaviour, since peak potentials vary with scan rate and resulting CV shapes can broaden significantly. As a result, the E_{ox} and E_{red} potentials are determined at the potential where the current increases substantially (i.e., onset potential), which corresponds to the first injection of holes or electrons into the HOMO and LUMO, respectively [45, 58]. FTO|SnO_2|**BPTI-A** exhibits a broad, featureless reduction ($E_{red} = - 0.23$ V vs. NHE), experiencing a 40 mV shift compared to **BPTI-A** in solution. In contrast,

the FTO|SnO$_2$|**BPTI-B** system affords a relatively sharp 1st reduction at E_{red} = − 0.17 V *vs.* NHE, with a 20 mV shift higher potential than the dye in solution, much less than that observed for **BPTI-A** upon sensitization. The interaction and aggregation of the **BPTIs** on the SnO$_2$ surface result in a LUMO with lower energy and is more evident in the stronger aggregating **BPTI-A**. The down-shift and broadness of the redox level result from the formation of semiconductor-like continuous energy levels when the molecules were stacked, rather than the discrete energy levels found in isolated molecules [46]." This opens the possibility that additional aggregation could yield a more stable radical-anion species, also observed in **PDI** aggregation in solution and films [59]. The stable radical anion was confirmed by spectroelectrochemical studies (SI, Section S12, **Figure S25**) by showing electrochromism[60] and might enhance the injection probabilities of excited dye into the semiconductor [38, 39]. Further evidence of aggregation was found in the UV–Vis spectra of **BPTI** upon SnO$_2$ sensitization shown in Fig. 1C and summarized in Table 1.

The spectra reveal a considerable broadening of all absorbances, extending the light-harvesting properties of the **BPTI**–SnO$_2$ composites further into visible wavelengths. Although the absorbance maxima remains unchanged compared to solution data, the shapes and onset of the spectra show significant differences. Different aggregation modes can explain the change in photophysical properties, as shown in Scheme 2 and SI Section S8–9, and **Figure S22–S23**. The onset of absorption for **BPTI-A** experiences a significant bathochromic shift from ~ 500 nm (solution) to ~ 550 nm (SnO$_2$). This considerable enhancement to longer-wavelength absorption over **BPTI-B** on SnO$_2$ (~ 515 nm) should translate to enhanced light harvesting in solar cells and photoelectrochemical devices (vide infra).

2.5 Aggregation behavior of the BPTIs

Depending on the orientation angle of the perylene assemblies (SI, Section S8), features of *J*-aggregates (head-to-tail) or *H*-aggregates (face-to-face) can emerge. Interestingly, perylenes with an orientation angle between both modes demonstrate a combination of both characteristics (which we refer to as *X*-aggregates[35]) [15, 61].
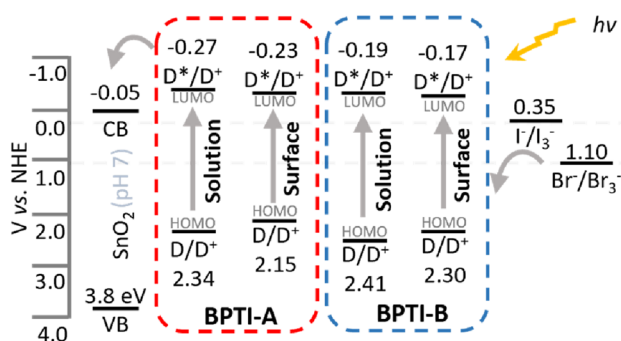
The significant red shift of absorbance in the solid state (i.e., as observed for **BPTI-A**) is often assigned to *J*-aggregation [41]. In *J*-aggregation, the head-to-tail alignment within an ordered aggregate enhances the dipole moment relative to the monomeric dye, leading to a larger transition dipole moment after absorption and stabilization of the excitation band, causing the bathochromic shift (Scheme 1C). In contrast to the behavior of **BPTI-A**, the

vast majority of **PBI** dyes exhibit blue-shifting of absorbance in the solid-state originating from *H*-aggregation [62], where dyes are stacked in a face-to-face orientation (Scheme 1C). This mode of aggregation aligns transition dipole moments in a parallel fashion, making only one out of the two possible excitonic transitions allowed, forcing a preference for transition to the higher energy state that corresponds to a hypsochromically shifted or an "*H*-type band" [42, 44]. Evidence for the formation of *H*-type is seen in π-stacked **BPTI** aggregates from the intensity reversal of the 0–0 and 0–1 bands in the UV–Vis spectrum and is elaborated on in the SI in Section S9 [63, 64]. This enhancement in the 0–1 vibrational band is more apparent for **BPTI-A** than for **BPTI-B** (0–0/0–1 absorbance ratio = 0.93, 1.03 and ~ 1.45 for **BPTI-A**, **BPTI-B** on SnO$_2$ and monomeric **BPTIs**, respectively). Therefore, **BPTI-A** exhibits a combination of both aggregation modes by a significant red-shift on SnO$_2$ surfaces by way of *J*-aggregation accompanied by the reversal of vibrational-band absorbance intensity caused by *H*-aggregation phenomena. While **BPTI-B** also exhibits slight aggregation features, it is less pronounced, leading us to believe that this species is substantially present as a monomer. We surmise that the **BPTI** assemblies are not entirely placed face-to-face or head-to-tail but are angled in an in-between position as visualized in Scheme 1C and **Figure S22**.[61] These types of "*X*-aggregates" have been reported previously[15, 35] and are elaborated on in the SI, Section S8.

2.6 Excited-state stabilization by aggregate formation

Steady-state fluorescence spectra of **BPTI**–SnO$_2$ photoanodes revealed significant changes compared to these spectra obtained from solution measurements, as seen in Fig. 1C − D and summarized in Table 1. It should be noted that the **BPTI** dyes emissive behavior even after being immobilized on the SnO$_2$ surface suggests that there is limited electron injection into the SnO$_2$ semiconductor since the excited state is not completely quenched leading to less effective photoelectrochemical cells. A significant red-shift of the emission maximum was observed from 485 nm in solution to 580 nm and 560 nm, respectively, for FTO|SnO$_2$|**BPTI-A** and **BPTI-B**. These experiments show a large Stokes shift (**BPTI-A** 18 nm → 115 nm), suggesting that excited-state relaxation is more effective in the **BPTI** aggregates [44]. Notably, the well-resolved vibronic features in solution spectra coalesce into a broad, featureless emission from the SnO$_2$ surface, consistent with previous reports of *H*-aggregation [31]. The consistent position between monomeric (solution) and aggregated (solid-state) species in absorbance maxima contrasts the large red shift experienced in emission maxima between the **BPTIs**. Since red-shift results from lower-lying

excited states, this indicates that higher degrees of aggregation endow greater stabilization to excited electrons than monomeric species (SI, Section S9 and **Figure S23**) [65]. We speculate that enhanced exciton may influence excited state dynamics to potentially create an advantageous pathway for improved electron injection at the photoanode, leading to better photovoltaic performance [66]. This speculation could be supported by the observation that in **PDI** dimers and higher aggregates, the low-lying excited states result from the delocalization of excitation energy over multiple chromophores throughout the π-system [67]. The optical gap was estimated with the E_{0-0} using absorption and emission data of immobilized **BPTIs**, revealing a significant decrease from ~ 2.60 eV (monomeric) to 2.38 eV (**BPTI-A**) and 2.47 eV (**BPTI-B**) on FTO|SnO$_2$. As we could not ascertain an E_{ox} of the dye on FTO|SnO$_2$|**BPTI** electrodes, we used the optical gap with the electrochemically determined E_{red} (i.e., estimated LUMO level) to estimate the E_{ox} (i.e., estimated HOMO level) of the surface-mounted dyes. The decrease in optical gap coupled with the shift of the 1st reduction to lower potentials decreases the estimated E_{ox} to 2.15 V

and 2.30 V *vs*. NHE for **BPTI-A** and **BPTI-B**, respectively. While this oxidative power is still exceptional, the decrease of E_{ox} upon aggregation is something to be mindful of when designing dye-sensitized systems. Together, these experimental observations suggest that the alkyl group of **BPTI-A** exerts a minimal electronic influence while demonstrating a significant influence in self-assembly. Thus, given the optical and electronic similarity between the two monomeric **BPTI** dyes, the difference in spectroscopic features on the FTO|SnO$_2$ plates is mainly due to aggregation behavior. Importantly, aggregates can accommodate mobile excitons with a π–π* character upon light absorption that can facilitate electron injection at the semiconductor surface [27], implying that **BPTI**-dye aggregates can potentially outperform its monomeric species in a photoelectrochemical device.

Furthermore, in combination with the electrochemical data, we can conclude that the use of SnO$_2$ ($E_{CB} = -0.05$ eV) over TiO$_2$ ($E_{CB} = -0.5$ eV) is required for **BPTI** dyes to facilitate exergonic electron injection upon light absorption. It is important to note that the aggregation behavior is not unique to immobilized dyes on SnO$_2$, as comparable data were obtained for these dyes immobilized on TiO$_2$ (**Figure S14B**). Therefore, the changes to fluorescence spectra are a result of dye-based phenomena and are not caused by dye–semiconductor interactions. From the solution data, we can create an energy diagram to rationalize the operation of DSSCs and DSPECs with **BPTI** photoanodes (Scheme 3).

Scheme 3 Energy level diagram of **BPTI-A** and **BPTI-B** on SnO$_2$ combined with the I$^-$/I$_3^-$ and Br$^-$/Br$_3^-$ redox mediator couples. D/D$^+$ and D*/D$^+$ are represented by the HOMO and LUMO levels, respectively and are calculated using the formula HOMO = LUMO + E_{0-0} [51], with the first reduction potential (E_{red}) corresponding to the LUMO level, which is estimated based on the formal (solution-based) or the onset (sensitized systems) potential [45]

2.7 Influence of BPTI aggregation on photocurrent density in DSSCs

Having established the role of structure in promoting aggregation phenomena during **BPTI** dyes adsorption, we turned our efforts to applying these photoanodes in photoelectrochemical devices. Therefore, dye loading on the **BPTI** photoanodes was quantified to enable a fair comparison of photovoltaic properties. **BPTIs** were leached of freshly sensitized FTO|SnO$_2$|**BPTI** plates by adding them to a 0.01 M

Table 2 Data of FTO|SnO$_2$|**BPTI-A** and **BPTI-B** sandwich DSSC devices with a standard deviation of $N = 3$ in brackets

Entry	Dye	Redox couple	J_{sc} (mA cm^{-2})	V_{oc} (V)	FF	η (%)
1	**BPTI-A**	I$^-$/I$_3^-$ MeCN	1.24 ($\pm$0.057)	0.16 ($\pm$0.009)	0.45 ($\pm$0.014)	0.12 ($\pm$0.003)
2	**BPTI-B**	I$^-$/I$_3^-$ MeCN	0.28 ($\pm$0.022)	0.13 ($\pm$0.002)	0.42 ($\pm$0.004)	0.02 ($\pm$0.001)
3	**BPTI-A**	Br$^-$/Br$_3^-$ MeCN	0.46 ($\pm$0.024)	0.38 ($\pm$0.013)	0.61 ($\pm$0.012)	0.11 ($\pm$0.006)
4	**BPTI-B**	Br$^-$/Br$_3^-$ MeCN	0.07 ($\pm$0.011)	0.36 ($\pm$0.008)	0.62 ($\pm$0.012)	0.02 ($\pm$0.003)
5	**BPTI-A**	Br$^-$/Br$_3^-$ Aqueous	0.34 ($\pm$0.010)	0.36 ($\pm$0.013)	0.52 ($\pm$0.102)	0.06 ($\pm$0.017)
6	**BPTI-B**	Br$^-$/Br$_3^-$ Aqueous	0.06 ($\pm$0.008)	0.28 ($\pm$0.022)	0.43 ($\pm$0.076)	0.01 ($\pm$0.003)

(WE = FTO|SnO$_2$|**BPTI-A** or **BPTI-B**, CE = FTO Pt electrodeposited, electrolyte: 0.5 M LiI or LiBr, 0.05 M I$_2$ or Br$_2$ in MeCN or 0.4 M LiBr, 0.05 M Br$_2$, 0.1 M HBr in H$_2$O (pH = 0.54), 0.07 cm^2 mask, illuminated with a 100 mW cm^{-2} white light source, Figure S16)

TBAOH in DMF solution, then acquiring absorbance spectra (**Figure S12**). An extended discussion on possible binding modes of the dye to the SnO_2 surface is found in the SI Section S11 [68]. Notably, these experiments ($N = 3$) show that the FTO|SnO_2|**BPTI-A** photoanode has a dye loading of 43 (± 3.0) nmol cm^{-2} while FTO|SnO_2|**BPTI-B** contains an ~ twofold lower dye loading of 23 (± 3.2) nmol cm^{-2}. A linear relationship between dye loading and photocurrent density is often seen in DSSCs [69], suggesting that a doubling of photocurrent density of **BPTI-A** DSSCs (compared to **BPTI-B**) would be easily rationalized by enhanced dye loading via (non-quenching) aggregation [70, 71]. DSSCs were constructed using **BPTI** photoanodes combined with electrodeposited Pt/FTO counter electrodes (CE) and an iodide/triiodide (I^-/I_3^-) redox couple in MeCN. A detailed account of device construction is given in the SI Section S5, with the results summarized in Table 2. The DSSCs are measured with a 100 mW cm^{-2} LED lamp as used in photosynthetic experiments and will be discussed further in the text, for literature references the DSSCs were also measured under 1 sun (Table S1B, AM1.5G, 100 mW cm^{-2}) to allow literature comparison (Figure S16). All DSSCs are prepared and measured in similar time frames and were remeasured directly after preparation and after 1 week (Table S1). Both **BPTI**-based DSSCs (Table 2, Entry 1 and 2) exhibited similar open-circuit voltage (V_{OC}) of ~ 0.16 V and Fill Factors (FF) ~ 0.42, suggesting both DSSCs are regenerated in the same manner by the redox electrolyte. The comparable V_{OC} suggests a negligible change in the Fermi-level of the CB upon dye adsorption, implying that the monolayer coverage of **BPTIs** is comparable between photoanodes as the same amount of H^+ from carboxylic acid anchor intercalates and lowers the Fermi-level (which lowers the V_{OC}) by the same amount [72]. Remarkably, DSSCs employing the highly aggregating **BPTI-A** experience a ~ 5 × increase in short-circuit photocurrent density (J_{sc}) of 1.24 mA cm^{-2}, over the monomeric **BPTI-B** 0.28 mA cm^{-2}. Having revealed the beneficial effect of aggregation of the **BPTI-A** dye in standard DSSCs, we explored the use of the bromide/tribromide (Br^-/Br_3^-) redox couple in MeCN to assess if the E_{ox} of the **BPTI** dyes is capable of oxidizing Br^- and accessing higher photovoltage [23]. Again, the J_{sc} of DSSCs based on **BPTI-A** (0.46 mA cm^{-2}, Entry 3) was about 6 × higher than those based on **BPTI-B** (0.07 mA cm^{-2}, Entry 4), while improvements in V_{OC} were realized for both systems through the use of a higher potential redox couple. Finally, to assess the possibility of realizing DSPECs-based Br_2 production, we explored the (Br^-/Br_3^-) RM in 0.1 M HBr aqueous solutions to imitate the (acidic) photoanode environment used in photosynthetic experiments. The low pH (0.54) of this aqueous SnO_2-based DSSCs is necessary as greater proton content shifts the Fermi-level of the SnO_2 to more positive potentials, increasing the required driving force for charge injection from the **BPTIs** into SnO_2 [27]. The acidic pH may dissolve MO_x, but no decrease in photovoltaic performance were observed in our DSSCs over a week (Table S4), suggesting stability for our window of photosynthetic testing. A similar sixfold increase in J_{sc} was observed for acidic aqueous Br^-/Br_3^- DSSCs with **BPTI-A** (0.34 mA cm^{-2}) compared to those based on **BPTI-B** (0.06 mA cm^{-2}). To summarize, DSSCs that employ **BPTI-A** as a sensitizer have a photocurrent density that is ~ 5 × more than when using better **BPTI-B** with just double the dye loading, and the improvement is independent of the electrolyte.

2.8 Electrochemical impedance spectroscopy and incident photon-to-current efficiencies studies

According to our dye loading studies, only a twofold in J_{sc} is expected (SI, Section S13), while here, a 5–sixfold (electrolyte dependent) increase in J_{sc} is obtained using the self-assembling **BPTI-A**. To better understand the significant increase in efficiency between DSSCs with **BPTI-A** and **BPTI-B**, electrochemical impedance spectroscopy (EIS) was employed and analyzed in the SI (Section S15, Table S4, Figure S28–29), although the research on the application of EIS analysis to model electron transport behavior in SnO_2-based DSSCs is limited [73]. Insights into electron–hole recombination at the semiconductor–dye interface were sought through EIS measurements taken at varying light intensities [74]. Electron lifetime (τ_e) as a function of V_{OC} was assessed to explore differences in recombination resistance (R_{rec}) or chemical capacitance ($C\mu$) caused by a shift in the conduction band. The resulting data showed an increase of τe (I^-/I_3^- MeCN at 0.14 V: 100 and 130 ms, Br^-/Br_3^- MeCN at 0.3 V: 63 and 118 ms and Br^-/Br_3^- in aqueous solution pH 0.54 at 0.25 V: 36 and 78 ms for **BPTI-A** and **BPTI-B**, respectively, Table S4, Figure S28A) for DSSCs prepared with **BPTI-B** compared to **BPTI-A**. This finding was attributed to a difference in R_{rec}, rather than a conduction band shift since the $C\mu$ did not change when comparing DSSCs with **BPTI-A** and **BPTI-B** (Figure S28B) [73]. Interestingly, while the measured R_{rec} for **BPTI-B** was higher than for **BPTI-A** (Figure S28C, Table S4), the improvement in cell efficiency was reversed. This indicates that recombination suppression by aggregation of **BPTI-A** did not contribute to the enhanced cell efficiencies observed.

$$IPCE = \varphi_{inj} \times \eta_{coll} \times LHE \qquad (5)$$

As a positive effect of aggregation, we surmise that the increased π-stacking of **BPTI-A** leads to a more stabilized excited state through electron delocalization [70, 71] (SI, Section S13, and **Figure S26**), resulting in higher electron injection efficiency (φ_{inj}). Additionally, the increased visible
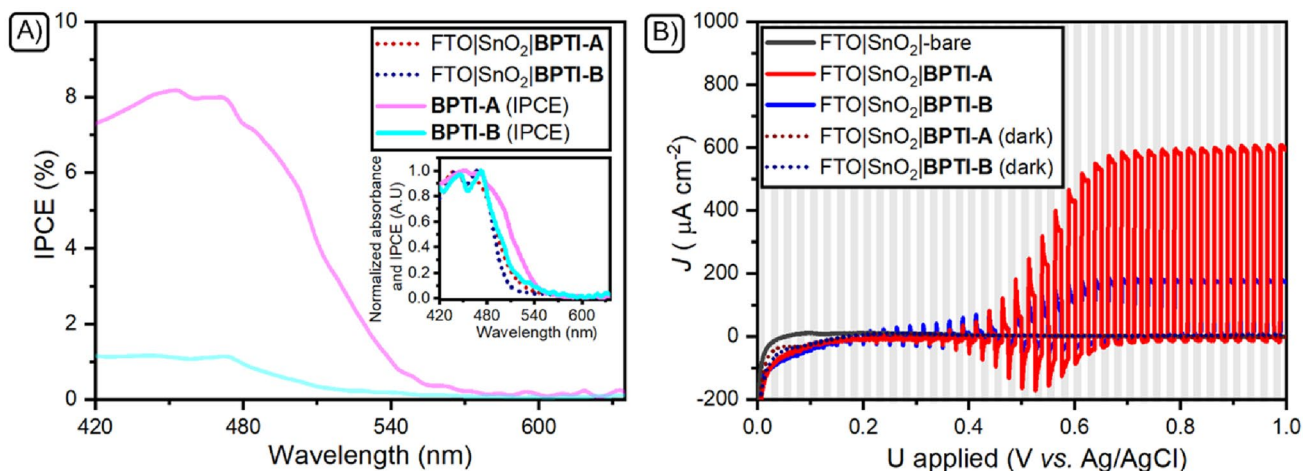
Fig. 2 A IPCE of DSSCs with **BPTI-A** (pink) and **BPTI-B** (cyan) and the I^-/I_3^- couple in MeCN. Insert the normalized IPCE spectra to observe the wavelength-dependent light-harvesting efficiency with absorbance spectra of FTO|SnO$_2$|**BPTI-A** (dark red dotted), and **BPTI-B** (dark blue dotted) as a reference. Measurements are shown from 420 nm to prevent direct bandgap excitation of SnO$_2$. **B** Chopped light experiments with varying applied potential with 5 s light on (white background) and 5 s off (grey background) WE: FTO|SnO$_2$|**BPTI-A** (red) or **BPTI-B** (blue) 0.1 M HBr, 1.0 M LiBr in H$_2$O (3 mL), CE: FTO|Pt, 0.01 M HBr, in H$_2$O (3 mL), separated by Nafion-117 proton exchange membrane, masked area = 0.64 cm^2 and illuminated with a LED light source (Zahner, TLS3, 100 mW cm^{-2}, **Figure S16**)

light absorbance would increase the light-harvesting efficiency (*LHE)*. These features were accessed by measuring incident photon-to-current efficiencies (IPCE, Eq. 5) [27, 34]. The IPCE spectra were normalized to study the wavelength-dependent light-harvesting efficiency as shown in Fig. 2A of the **BPTI**-DSSCs with I^-/I_3^- (Br^-/Br_3^-, **Figure S26 C–F**). The absorption bands of the 0–0 and 0–1 transition are well resolved for **BPTI-B**, and consistent with the corresponding absorption spectra of the thin films and their overall monomeric behavior. In contrast, the IPCE of the **BPTI-A**-based DSSC affords a broad photocurrent action spectrum (i.e., no vibrational features), with the enhanced red-light harvesting efficiency anticipated from UV–Vis spectra of the dye on SnO$_2$. Importantly, although the beneficial aggregation phenomenon occurring in **BPTI-A** devices can partly explain increased J_{sc}, it does not account for the > fivefold improvement. The maximal IPCE, visible in the insert of Fig. 2A, of the DSSC with **BPTI-A** shows a ~ fourfold improvement compared to **BPTI-B**. We surmise that, within this system, collection efficiency (η_{coll}, the collection efficiency of electrons back of the photoactive electrode) is not improved by using different dyes, but only by the injection of more electrons and is further suggested by EIS (Table S4). The remaining improvement in IPCE in the DSSCs using the more aggregating **BPTI-A** can only be a result of an increased φ_{inj}. Various suggestions on the reasoning behind enhanced electron injection are further elaborated in the SI Section S13.

Even though the positive effects of aggregation are clearly visible, we also explored the losses that contributed to aggregation. The negative effects of dye aggregation are typically observed in DSSCs by photocurrent dynamics, i.e., the non-linearity of photocurrent upon variation of the light intensity (elaborated in the SI Section S14, **Figure S27**). Although some disadvantage due to aggregation of the **BPTIs** is seen, the amount of aggregation does not seem to influence this behavior. Studies on the fluorescence lifetime and binding geometry of the **BPTIs** are clearly of interest to the reason for the enhanced electron injection. Concluded, the fivefold increase in photocurrent production using **BPTI-A**, is surmised to be a result of a higher dye loading (twofold), and the rest is thanks to increased *LHE* by broader wavelength and enhanced φ_{inj}.

2.9 Influence of BPTI aggregation on the performance of the bromine production in the DSPECs

The light-driven oxidation of Br^- to Br_2 was examined using a DSPEC photoreactor (**Figure S18**) with the dye-sensitized photoanode as the working electrode, Ag/AgCl reference electrode, and Pt-FTO counter electrode. An HBr/LiBr anolyte and HBr catholyte were used, separated by a Nafion-117 membrane. Previously, HBr splitting in SnO$_2$-based DSPECs have demonstrated decreasing J_{sc} with increasing pH. Therefore, an aqueous HBr solution with pH = 0.54 was selected (The same pH as the DSSC described before) [27]. Experimental details on the photoreactor components, assembly, and measurements are found in the SI Section S7. The bias potential was determined to be

Table 3 Control reactions in DSPECs with FTO|SnO$_2$|**BPTI-A** or **BPTI-B** were performed for $t = 16$ h

Entry	System	Conversion based on photocurrent (½ μmol electrons)	Br$_3^-$/Br$_2$(μmol)	FE (%)
1	FTO|SnO$_2$|-bare	0.017	0	–
2	FTO|SnO$_2$|**BPTI-A** (dark)	0.005	0	–
3	FTO|SnO$_2$|**BPTI-B** (dark)	0.001	0	–
4	FTO|SnO$_2$|**BPTI-A**	47	46.40 ($\pm$1.313)	99
5	FTO|SnO$_2$|**BPTI-B**	8.4	6.57 ($\pm$0.210)	79

*Faradaic efficiency was not obtained for a system with a photocurrent near 0 μmol

The cell was filled with 0.1 M HBr, 1.0 M LiBr in H$_2$O (3 mL). Bias potential was set to 700 mV *vs.* Ag/AgCl, and the system was illuminated with a 100 mW cm^{-2} white LED light source (masked size 0.64 cm^2, Figure S16)

700 mV *vs.* Ag/AgCl by chopped-light voltammetry, which is in the range of other HBr splitting SnO$_2$-based DSPECs. [27]. Under these conditions, the system based on the aggregating **BPTI-A** reveals a ~ fivefold increase in photocurrent density over devices based on the less aggregating **BPTI-B**, consistent with DSSC experiments (Fig. 2B). Furthermore, no dye leach was observed from the SnO$_2$ plates after long-term illumination (**Table S2**), demonstrating good photoanode stability in the time window used. The devices only produced quantifiable Br$_3^-$/Br$_2$ if the photoanode was illuminated (**Figure S20**) and **BPTI-A** or **BPTI-B** was present on the SnO$_2$ surface (see Table 3). The long-term performance on Br$^-$ oxidation over 16 h of illumination shows an average photocurrent density of 300 and 60 μA cm^{-2} for systems based on FTO|SnO$_2$|**BPTI-A** and **BPTI-B,** respectively. (**Figure S19**). Anolyte sampling determined 46.40 μmol and 6.57 μmol of photoproduced Br$_3^-$/Br$_2$ in the DSPECs based on **BPTI-A** and **BPTI-B,** respectively, leading to Faradaic efficiencies of 99 and 79%. Finally, GC sampling of the catholyte headspace revealed H$_2$ as the only reduction product completing the solar-to-fuel system (**Figure S21**). No further research was done on the cathodic side since the focus of this study is on the light-driven elements of the DSPEC and the generation of H$_2$ on Pt electrodes is well-established [75–77] and known for DSPECs [78, 79] with FE up to 90% [80].Compared to literature reports that use Ru(polypyridyl) complexes in related devices, with Faradaic efficiency of 14% in Br$_3^-$/Br$_2$ production, the DSPECs using **BPTI-A** and **BPTI-B** reported here display much high efficiencies [22]. In conclusion, a DSPEC photoreactor equipped with a dye-sensitized photoanode was used to study the light-driven oxidation of Br$^-$to Br$_2$. The system based on aggregated **BPTI-A** demonstrated a ~ fivefold increase in product production thanks to better photovoltaic performance.

3 Conclusion

Two novel dyes, **BPTI-A** and **BPTI-B** were synthesized, differing in imide substituents that respectively promote (alkyl) or suppress (aryl) aggregation by π-stacking. Optical and electrochemical characterization of the **BPTIs** revealed properties identical in solution (i.e., monomeric species) but are very different when adsorbed onto SnO$_2$ as this induced aggregation. Specifically, **BPTI-A** experienced significant perturbation of redox properties, absorption, and emission diagnostic upon the formation of self-assembled aggregates. The FTO|SnO$_2$|**BPTI-A** photoanode experienced a 50 nm enhancement in light-harvesting absorption and a twofold increased dye loading compared to less π-stacking **BPTI-B.** Although general photovoltaic properties are low, the increased dye loading, stabilization of the excited state, and the red-shift of the absorption properties of **BPTI-A** give an approx. fivefold increase in photocurrent density in DSSCs combined with the I$^-$/I$_3^-$ and the Br$^-$/Br$_3^-$-couple in MeCN and acidic aqueous solutions compared to DSSCs prepared with more monomeric **BPTI-B**. Light-driven production of the strong oxidant Br$_2$ was achieved in DSPECs with photoanodes sensitized with **BPTI-A** and **BPTI-B**. The DSPECs with aggregating **BPTI-A** outperformed **BPTI-B** by a nearly sixfold increase in Br$_2$ production. The increase in performance was further studied with Electrochemical Impedance Spectroscopy which showed that suppressed electron recombination from the semiconductor to the electrolyte is not the main cause of enhanced cell performance. Incident Photon-to-Current Efficiencies studies indicate that the increased electron injection efficiency combined with a larger light harvesting efficiency are the major causes for cell improvement when using the aggregating **BPTI-A**. Our findings suggest that self-assembly can be an effective technique in optimizing the light absorption and charge separation properties of dye-sensitized devices. While it is typically considered that aggregation-based quenching detracts from photovoltaic performance in DSSCs, this work demonstrates an example of how aggregation can improve photovoltaic performance and product yield. By enhancing aggregate forming and

hydrophobicity in the dyes, photoanodes can be developed to withstand harsh aqueous environments. This could pave the way for the creation of stable devices that facilitate high-potential aqueous solar fuel generation in the long term.

4 Experimental section

4.1 Materials, methods and devices

A complete elaboration on the materials, devices, and methods used is given in the Supplementary Information in Section S1 and S2.

4.2 Synthesis of photosensitizers

BPTI-A and BPTI-B. BPTI-A and **BPTI-B** were synthesized by adapting literature procedures for similar **PDI** and **BPTI** modifications [38, 39]. A complete elaboration on the dye synthesis, characterization and solvatochromism is given in Supplementary Information Section S3, S10.

5 Photoanode and counter electrode preparation

A complete elaboration on the (photo)electrode preparation and characterization is given in Supplementary Information Sections S4 and S12. FTO electrodes (Solaronix, 2.2 mm, $15\,\Omega\,\mathrm{sq}^{-1}$) ($10\times5$ cm) were cleaned. A SnO_2 blocking layer was added by immersing the plates into an aqueous $SnCl_4$ solution (40 mM, 100 mL) for 30 min at 70 °C, after which the plates were rinsed with ethanol and sintered at 500 °C. Two mesoporous active layers of SnO_2 nanoparticles (SnO_2 paste was prepared similar to literature procedures [81], particle size 22–42 nm, WAKO) were screen printed (0.79 cm^2 circles for DSPECs, 0.19 cm^2 circles for DSSCs) the thickness of the layer after annealing at 500 °C was 6.1 μm with a surface area of 36.2 m^2 g^{-1}. (**Figure S11**) The FTO|SnO$_2$ electrodes were sensitized with < 0.25 mM **BPTI-A** (near saturation) or 0.25 mM **BPTI-B** in a 1:1 *t*-BuOH/THF solution in the dark overnight, giving a yellow color to the semiconductor in the plates. The plates were rinsed afterward with a 1:1 *t*-BuOH/THF solution and kept in the dark. Counter electrodes were prepared with clean FTO electrodes (Solaronix, 2.2 mm, $15\,\Omega\,\mathrm{sq}^{-1}$), after which a platinum layer was added by electrochemical deposition of platinum.

6 Preparation of DSSCs

A complete elaboration on the DSSC preparation is given in Supplementary Information Section S5. Sensitized SnO_2 photoanodes and Pt counter electrodes were sandwiched together using a hotmelt ionomer, after which the electrolyte (0.5 M LiI/LiBr 0.05 M I$_2$/Br$_2$ in MeCN or 0.4 M LiBr, 0.05 M Br$_2$, 0.1 M HBr in H$_2$O) was introduced into the cells by vacuum backfilling, and the cells were sealed. The DSSCs were measured using a P211 potentiostat (Zahner TLS3, 100 mW cm^{-1} LED lamp, **Figure S16**) using a 0.07 cm^2 mask. The set-up of IPCE, photodynamic, and EIS studies are further elaborated in the Supporting information Sections S13–S15.

7 Photoelectrochemical setup for photosynthetic experiments

A complete elaboration on the DSPEC preparation is given in Supplementary Information Section S7. The photoreactor (**Figure S11**) comprises 2 Teflon compartments separated by a Nafion-117 membrane (FuelCellStore). The working electrode compartment (WEC) contained the photoanode (masked size 0.64 cm^2) as the WE, an Ag/AgCl (leakless, eDAQ, ET069) RE and filled with a solution of 0.1 M HBr, 1.0 M LiBr in H$_2$O (pH ~ 0.5, 3 mL). The counter electrode compartment (CEC) contained an electrode with Pt electrodeposited on FTO and was filled with the same solution. Chopped-light experiments at various applied potentials were performed with 5 s of illumination on a P211 potentiostat (Zahner) with a white light LED light source (Zahner, TLS3, 100 mW cm^{-2}, **Figure S16**). Long-term chrono-amperometric photocurrent measurements at 700 mV *vs.* Ag/AgCl were obtained with the same setup, and samples of the WEC were taken after the measurement. The formation of Br$_2$ was monitored with UV–Vis (elaborated on in the SI Section S6). The counter electrode compartment was attached to a Gas GC to measure H$_2$ evolution. The integration of half the photocurrent determines the number of electrons to account for two electrons needed per oxidation reaction (*i.e.* 2 Br$^-$ + 2e$^-$ → Br$_2$).

Declarations

References

1. H. Ritchie, M. Roser, *Our World in Data* **2020**.
2. K. Scott, in *RSC Energy and Environment Series*, The Royal Society Of Chemistry, **2020**, pp. 1–27.
3. Blankenship, R. E. (2008). *Molecular Mechanisms of Photosynthesis*. Wiley.
4. Zhang, B., & Sun, L. (2019). *Chemical Society Reviews, 48*, 2216.
5. O'Regan, B., & Grätzel, M. (1991). *Nature, 353*, 737.
6. Mathew, S., Yella, A., Gao, P., Humphry-Baker, R., Curchod, B. F. E., Ashari-Astani, N., Tavernelli, I., Rothlisberger, U., Nazeeruddin, M. K., & Grätzel, M. (2014). *Nature Chemistry, 6*, 242.
7. Kakiage, K., Aoyama, Y., Yano, T., Oya, K., Fujisawa, J. I., & Hanaya, M. (2015). *Chemical Communications, 51*, 15894.
8. Grätzel, M. (2001). *Nature, 414*, 338.
9. Brennaman, M. K., Dillon, R. J., Alibabaei, L., Gish, M. K., Dares, C. J., Ashford, D. L., House, R. L., Meyer, G. J., Papanikolas, J. M., & Meyer, T. J. (2016). *Journal of the American Chemical Society, 138*, 13085.
10. Yun, S., Vlachopoulos, N., Qurashi, A., Ahmad, S., & Hagfeldt, A. (2019). *Chemical Society Reviews, 48*, 3705.
11. Zhang, S., Ye, H., Hua, J., & Tian, H. (2019). *EnergyChem, 1*, 100015.
12. Xu, P., & Mallouk, T. E. (2019). *Journal of Physical Chemistry C, 123*, 299.
13. Matheu, R., Garrido-Barros, P., Gil-Sepulcre, M., Ertem, M. Z., Sala, X., Gimbert-Suriñach, C., & Llobet, A. (2019). *Nature Reviews Chemistry, 3*, 331.
14. McCool, N. S., Swierk, J. R., Nemes, C. T., Saunders, T. P., Schmuttenmaer, C. A., & Mallouk, T. E. (2016). *ACS Applied Materials & Interfaces, 8*, 16727.
15. Bialas, D., Kirchner, E., Röhr, M. I. S., & Würthner, F. (2021). *Journal of the American Chemical Society, 143*, 4500.
16. Kamire, R. J., Materna, K. L., Hoffeditz, W. L., Phelan, B. T., Thomsen, J. M., Farha, O. K., Hupp, J. T., Brudvig, G. W., & Wasielewski, M. R. (2017). *Journal of Physical Chemistry C, 121*, 3752.
17. Yamamoto, M., Wang, L., Li, F., Fukushima, T., Tanaka, K., Sun, L., & Imahori, H. (2016). *Chemical Science, 7*, 1430.
18. Zhao, Y., Swierk, J. R., Megiatto, J. D., Sherman, B., Youngblood, W. J., Qin, D., Lentz, D. M., Moore, A. L., Moore, T. A., Gust, D., & Mallouk, T. E. (2012). *Proc Natl Acad Sci U S A, 109*, 15612.
19. Wang, D., Sampaio, R. N., Troian-Gautier, L., Marquard, S. L., Farnum, B. H., Sherman, B. D., Sheridan, M. V., Dares, C. J., Meyer, G. J., & Meyer, T. J. (2019). *Journal of the American Chemical Society, 141*, 7926.
20. Sheridan, M. V., Wang, Y., Wang, D., Troian-Gautier, L., Dares, C. J., Sherman, B. D., & Meyer, T. J. (2018). *Angewandte Chemie International Edition, 57*, 3449.
21. Bruggeman, D. F., Mathew, S., Detz, R. J., & Reek, J. N. H. (2021). *Sustain Energy Fuels, 5*, 5707.
22. Turlington, M. D., Brady, M. D., & Meyer, G. J. (2021). *ACS Appl Energy Mater, 4*, 745.
23. Bagheri, O., Dehghani, H., & Afrooz, M. (2015). *RSC Advances, 5*, 86191.
24. Wang, Z. S., Sayama, K., & Sugihara, H. (2005). *Journal of Physical Chemistry B, 109*, 22449.
25. Brady, M. D., Troian-Gautier, L., Sampaio, R. N., Motley, T. C., & Meyer, G. J. (2018). *ACS Applied Materials & Interfaces, 10*, 31312.
26. Liu, X., Chen, Z., Xu, S., Liu, G., Zhu, Y., Yu, X., Sun, L., & Li, F. (2022). *Journal of the American Chemical Society, 144*, 19770.
27. Benazzi, E., Rettenmaier, K., Berger, T., Caramori, S., Berardi, S., Argazzi, R., Prato, M., & Syrgiannis, Z. (2020). *Journal of Physical Chemistry C, 124*, 1317.
28. Park, H., Bae, E., Lee, J. J., Park, J., & Choi, W. (2006). *Journal of Physical Chemistry B, 110*, 8740.
29. Wang, D., Huang, Q., Shi, W., You, W., & Meyer, T. J. (2021). *Trends Chem, 3*, 59.
30. Lapides, A. M., Sherman, B. D., Brennaman, M. K., Dares, C. J., Skinner, K. R., Templeton, J. L., & Meyer, T. J. (2015). *Chemical Science, 6*, 6398.
31. Berardi, S., Cristino, V., Canton, M., Boaretto, R., Argazzi, R., Benazzi, E., Ganzer, L., Borrego Varillas, R., Cerullo, G., Syrgiannis, Z., Rigodanza, F., Prato, M., Bignozzi, C. A., & Caramori, S. (2017). *Journal of Physical Chemistry C, 121*, 17737.
32. Zhang, L., & Cole, J. M. (2017). *J Mater Chem A Mater, 5*, 19541.
33. Krasnovsky, A. A., & Bystrova, M. I. (1980). *Bio Systems, 12*, 181.
34. Cheema, H., Baumann, A., Loya, E. K., Brogdon, P., McNamara, L. E., Carpenter, C. A., Hammer, N. I., Mathew, S., Risko, C., & Delcamp, J. H. (2019). *ACS Applied Materials & Interfaces, 11*, 16474.
35. Ma, S., Liu, Y., Zhang, J., Xu, B., & Tian, W. (2020). *Journal of Physical Chemistry Letters, 11*, 10504.
36. Wang, Y. J., Li, Z., Tong, J., Shen, X. Y., Qin, A., Sun, J. Z., & Tang, B. Z. (2015). *J Mater Chem C Mater, 3*, 3559.
37. Kasha, M., Rawls, H. R., & El-Bayoumi, M. A. (1965). *Pure and Applied Chemistry, 11*, 371.
38. Chen, H. C., Hsu, C. P., Reek, J. N. H., Williams, R. M., & Brouwer, A. M. (2015). *Chemsuschem, 8*, 3639.
39. Chen, H. C., Williams, R. M., Reek, J. N. H., & Brouwer, A. M. (2016). *Chemistry - A European Journal, 22*, 5489.
40. Oleson, A., Zhu, T., Dunn, I. S., Bialas, D., Bai, Y., Zhang, W., Dai, M., Reichman, D. R., Tempelaar, R., Huang, L., & Spano, F. C. (2019). *Journal of Physical Chemistry C, 123*, 20567.
41. Würthner, F., Kaiser, T. E., & Saha-Möller, C. R. (2011). *Angewandte Chemie - International Edition, 50*, 3376.
42. Chen, Z., Fimmel, B., & Würthner, F. (2012). *Organic & Biomolecular Chemistry, 10*, 5845.
43. Türkmen, G., Erten-Ela, S., & Icli, S. (2009). *Dyes and Pigments, 83*, 297.
44. Chen, Z., (2006). π-Stacks Based on Self-Assembled Perylene Bisimides: Structural, Optical, and Electronic Properties, Thesis.
45. Veldman, D., Meskers, S. C. J., & Janssen, R. A. J. (1939). *Advanced Functional Materials, 2009*, 19.
46. Wang, J., Shi, W., Liu, D., Zhang, Z., Zhu, Y., & Wang, D. (2017). *Applied Catalysis, B: Environmental, 202*, 289.

47. Karuppuswamy, P., Chen, H., Wang, P., Hsu, C., Wong, K., & Chu, C. (2018). *Chemsuschem, 11*, 415.

48. Bard, R., Allen, J., & Faulkner, L. (2001) *Electrochemical Methods: Fundamentals and Applications*, John Wiley & Sons, Inc. ISBN: 978-0-471-04372-0

49. Hagfeldt, A., Boschloo, G., Sun, L., Kloo, L., & Pettersson, H. (2010). *Chemical Reviews, 110*, 6595.

50. Kirner, J. T., Stracke, J. J., Gregg, B. A., & Finke, R. G. (2014). *ACS Applied Materials & Interfaces, 6*, 13367.

51. Lindquist, R. J., Phelan, B. T., Reynal, A., Margulies, E. A., Shoer, L. E., Durrant, J. R., & Wasielewski, M. R. (2016). *J Mater Chem A Mater, 4*, 2880.

52. Karlsson, C., Huang, H., Strømme, M., Gogoll, A., & Sjödin, M. (2015). *RSC Advances, 5*, 11309.

53. Fuller, C. A., & Finlayson, C. E. (2017). *Physical Chemistry Chemical Physics, 19*, 31781.

54. Lee, S. K., Zu, Y., Herrmann, A., Geerts, Y., Müllen, K., & Bard, A. J. (1999). *Journal of the American Chemical Society, 121*, 3513.

55. Matthews, R., Swisher, J., Hutchins, K. M., & Pentzer, E. B. (2018). *Chemistry of Materials, 30*, 3571.

56. Calbo, J., Doncel-Giménez, A., Aragó, J., & Ortí, E. (2018). *Theoretical Chemistry Accounts, 137*, 27.

57. Korjenic, A., & Raja, K. S. (2019). *Journal of the Electrochemical Society, 166*, C169.

58. Cardona, C. M., Li, W., Kaifer, A. E., Stockdale, D., & Bazan, G. C. (2011). *Advanced Materials, 23*, 2367.

59. Dinleyici, M., Al-Khateeb, B., Abourajab, A., Uzun, D., Koyuncu, S., & Icil, H. (2021). *Journal of Photochemistry and Photobiology, A: Chemistry, 421*, 113525.

60. Wang, Q., Zakeeruddin, S. M., Cremer, J., Bäuerle, P., Humphry-Baker, R., & Grätzel, M. (2005). *Journal of the American Chemical Society, 127*, 5706.

61. Thorley, K. J., & Würthner, F. (2012). *Organic Letters, 14*, 6190.

62. Hestand, N. J., & Spano, F. C. (2018). *Chemical Reviews, 118*, 7069.

63. D'Anna, F., Marullo, S., Lazzara, G., Vitale, P., & Noto, R. (2015). *Chemistry - A European Journal, 21*, 14780.

64. Han, J. J., Shaller, A. D., Wang, W., & Li, A. D. Q. (2008). *Journal of the American Chemical Society, 130*, 6974.

65. Marcon, R. O., & Brochsztain, S. (2007). *Langmuir, 23*, 11972.

66. Yoo, H., Yang, J., Yousef, A., Wasielewski, M. R., & Kim, D. (2010). *Journal of the American Chemical Society, 132*, 3939.

67. Margulies, E. A., Shoer, L. E., Eaton, S. W., & Wasielewski, M. R. (2014). *Physical Chemistry Chemical Physics, 16*, 23735.

68. *Comment: The Doubling of the Dye Loading Would Imply Small Aggregates with an Average of Two.*, **n.d.**

69. Zhang, L., Yang, X., Li, S., Yu, Z., Hagfeldt, A., & Sun, L. (2020). *Solar RRL, 4*, 1900436.

70. We Cannot Exclude That a Different Orientation of the Respective BPDI Also Contributes to a Difference in Injection Efficiency, Which Was Previously Proposed for Porphyrin-Baseddyes., **n.d.**

71. Rochford, J., Chu, D., Hagfeldt, A., & Galoppini, E. (2007). *Journal of the American Chemical Society, 129*, 4655.

72. Boschloo, G., Häggman, L., & Hagfeldt, A. (2006). *Journal of Physical Chemistry B, 110*, 13144.

73. Zainudin, S. N. F., Abdullah, H., & Markom, M. (2019). *Journal of Materials Science: Materials in Electronics, 30*, 5342.

74. Bouwens, T., Bakker, T. M. A., Zhu, K., Hasenack, J., Dieperink, M., Brouwer, A. M., Huijser, A., Mathew, S., & Reek, J. N. H. (2023). *Nature Chemistry, 15*, 213.

75. Li, C., & Baek, J.-B. (2020). *ACS Omega, 5*, 31.

76. Hansen, J. N., Prats, H., Toudahl, K. K., Mørch Secher, N., Chan, K., Kibsgaard, J., & Chorkendorff, I. (2021). *ACS Energy Letters, 6*, 1175.

77. Guo, F., Macdonald, T. J., Sobrido, A. J., Liu, L., Feng, J., & He, G. (2023). *Advanced Science*. https://doi.org/10.1002/advs.202301098

78. Sherman, B. D., Sheridan, M. V., Wee, K.-R., Marquard, S. L., Wang, D., Alibabaei, L., Ashford, D. L., & Meyer, T. J. (2016). *Journal of the American Chemical Society, 138*, 16745.

79. Bruggeman, D. F., Bakker, T. M. A., Mathew, S., & Reek, J. N. H. (2021). *Chemistry - A European Journal, 27*, 218.

80. Bruggeman, D. F., Laporte, A. A. H., Detz, R. J., Mathew, S., & Reek, J. N. H. (2022). *Angewandte Chemie International Edition*. https://doi.org/10.1002/anie.202200175

81. Cheema, H., & Delcamp, J. H. (2019). *Chemistry A European Journal, 25*, 14205.